(Received 11 July 2025, Accepted 15 October 2025, Scheduled 24 October 2025)

Design and Wireless Communication Performance Based on Broadband Millimeter Wave Patch Antenna

Luoyong Xiang and Wen Chen*

Testing Department, Chongqing Academy of Information and Communications Technology, Chongqing 401336, China

ABSTRACT: The advancement of wireless communication has led to continuous innovation in antenna technology to satisfy the growing requirement for wireless communication. However, in wireless communication, antennas still face problems and challenges such as high power consumption and low adaptability. To address these issues, this study introduces magneto electric dipoles to optimize broadband millimeter wave patch antennas and uses metasurface optimization patches to ultimately design broadband dual-polarized millimeter wave metasurface antennas. In comparative tests at different temperatures, the gain of the broadband dual-polarization millimeter-wave meta-surface antenna reached a peak of 10.7 dBi at around 35 GHz at -50°C. At 0°C and 50°C, the gain reached a peak of 10.2 dBi and 8.5 dBi, respectively. The result shows that the designed antenna has high accuracy, gain, and strong stability in wireless communication, and also has certain anti-interference ability in different environments.

1. INTRODUCTION

Millimeter Wave Antenna (MWA) is a core component of 5G communication equipment, autonomous driving radar, and satellite communication systems, which uses multi-layer structures or special patch shapes to achieve broadband characteristics. Its beam is narrow and can concentrate signals in a specific direction, so Broadband Millimeter Wave Patch Antennas (BMWPAs) have advantages such as good anti-interference ability and high transmission efficiency [1, 2]. The size of the bandwidth directly affects the data transmission rate and spectral efficiency of communication systems. Although bandwidth can be expanded through design, it is still influenced by factors such as structure and environment [3].

The growing demand for communication has prompted researchers to optimize antenna design and adopt new technologies. For example, Wu et al. proposed an efficient broadband reflective array antenna based on non-radiative dielectric waveguide elements to utilize the inherent non-resonant characteristics of waveguides to achieve broadband performance. The antenna achieved 18 and 27 gain bandwidths at 1 dBi and 3 dBi, with a peak aperture efficiency of 45. Simulation and measurement have both verified that the design achieved broadband and higher efficiency utilizing a low-cost compact structure [4]. Junior et al. designed a dual frequency, circularly polarized, efficient antenna to improve the square patch problem. The experiment showed that the proposed antenna exhibited higher efficiency values, ranging from 0.57% to 1.12% [5]. Wan et al. proposed a multi-antenna covert communication system detection method based on gamma approximation to detect the illegal covert communication behavior of criminals in real time for subsequent processing. The effectiveness of the method was verified via simulation experiments [6]. Nagar et al. proposed a low-profile tri-band wearable antenna to address the issue of antenna wearability. The designed antenna operated at 2.4–2.59 GHz, 3.15–3.76 GHz, and 5.1–5.9 GHz, and the curvature radius had no effect on the functionality of the developed antenna, making it an ideal choice for human body measurement. This study has spurred additional research on low-cost felt substrate antennas for wireless body area networks [7]. Wang et al. proposed a wearable antenna sensor using an electromagnetic band gap array to address the issue of humidity levels around the human surface affecting comfort and overall health. The antenna's resonant frequency slowly decreased with the increase of relative humidity level in the environment, and the humidity sensitivity could reach 90 MHz/RH between 1.64 and 40 RH. The actual measurement results of the generated antenna sensor were very consistent, verifying its appropriateness for humidity monitoring in human areas [8]. Battaglia et al. proposed a new method for array antenna synthesis and beamforming constraints. This method was applicable to any layout and cell orientation diagram, transforming the design problem into a finite number of convex optimization problems. This method met the required specifications and had high practical value [9].

In summary, in Wireless Communication (WC), BMWPA suffers from loss issues caused by small bandwidth and size limitations. Therefore, this study introduces a Magneto Electric Dipole (MED) to optimize the antenna, designs it using dual-polarization, and introduces metasurface improvements to ultimately design a Broadband Dual-Polarized Millimeter Wave Metasurface Antenna (BDMW-MA). The paper aims to enhance the performance of antennas in WC by expanding and improving their bandwidth and patch placement, meeting the antenna requirements of broadband, high gain, low cross-polarization, and miniaturization in WC systems. The innovation of this research lies in combining magnetoelectric dipoles

* Corresponding author: Wen Chen (chenwenwest@163.com).

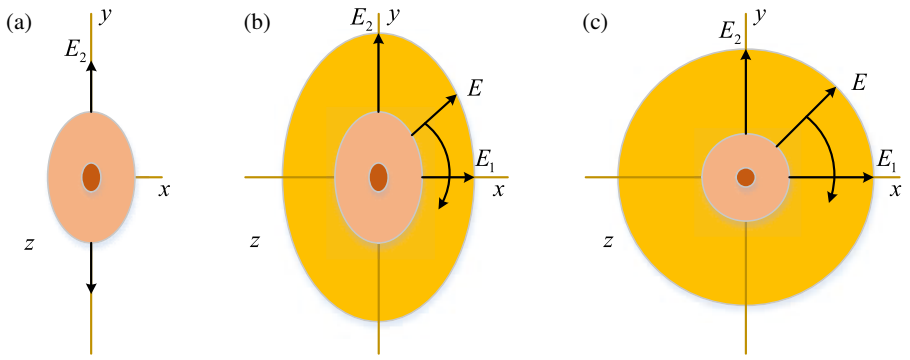

FIGURE 1. Antenna polarization. (a) Linear polarization. (b) Ellipsoidal polarization. (c) Circular polarization.

with metasurface technology to design a BDMW-MA. Compared to traditional microstrip antennas, the co-design of magnetoelectric dipoles addresses issues such as bandwidth limitations, single polarization, and poor gain stability. The dual-polarization optimization significantly improves overall transmission efficiency and enhances environmental stability. Compared to existing metasurface antennas, the co-optimization of metasurfaces and magnetoelectric dipoles enhances radiation efficiency and isolation, achieving high gain and dual-polarization characteristics.

2. METHODS AND MATERIALS

2.1. Construction of BDMW-MA Based on MED

BMWPA is widely used in 5G, Internet of Things (IoT), autonomous driving, and satellite communication, and participates in the operation of WC with its advantages of wide bandwidth and easy integration. However, traditional bandwidth expansion methods result in a significant increase in antenna size and weight, making it difficult to promote and apply in scenarios such as mobile devices and satellite communications, where size and weight are strictly limited [10, 11]. Therefore, by introducing MED, this study can achieve ultra-wideband performance, while the dual-polarization design of MED can achieve low cross-polarization and high isolation. Polarization is the spatial orientation and variation of electric field vectors in electromagnetic waves during propagation. Under different environments and conditions, electromagnetic waves may exhibit different polarization states, as shown in Fig. 1.

In Fig. 1(a), in linear polarization, the electric field vector always vibrates along a fixed direction, which is perpendicular to the propagation direction. In Fig. 1(b), elliptical polarization is an elliptical trajectory formed by the propagation of electric field vectors. In Fig. 1(c), circular polarization is a circular trajectory formed by the rotation of electric field vectors in a spiral manner during propagation. When the amplitudes of two orthogonal linearly polarized waves are not equal, and the phase difference is 90°, elliptical polarization will occur [12, 13]. For any polarization, it can be expressed as linear polarization components along the directions x and y, as shown in Equation (1).

$$\begin{cases} E_x = E_1 \sin(\lambda t - \lambda z) \\ E_y = E_2 \sin(\lambda t - \lambda z + \delta) \end{cases} \tag{1}$$

In Equation (1), E_x and E_y are the electromagnetic wave components in x and y. ω denotes the frequency of electromagnetic waves, and t is the time. λ is the phase constant, which is related to the medium's wavelength and refractive index. z is the position along the direction of electromagnetic wave propagation. δ is the phase difference, which represents the wave's phase delay or advance in the y direction relative to the wave in the x direction. In a dual-polarized antenna, these orthogonal electromagnetic wave components can coexist, allowing the antenna to operate in two different polarization directions simultaneously [14]. The antenna experiences energy loss due to polarization mismatch when receiving signals, as shown in Equation (2).

$$PLF = |\vec{e}^{\,*}_R \cdot \vec{e}|^2 \tag{2}$$

In Equation (2), $\vec{e}^{\,*}_R$ means the radiation wave potential vector of the antenna, and $\vec{e}$ denotes the wave potential vector of the radiation wave. The Polarization Loss Factor (PLF) is an important indicator for evaluating polarization matching performance. It represents the loss caused by polarization mismatch in antennas. The purpose is to evaluate and optimize the polarization matching performance of antennas during the design and analysis of antenna systems, thereby reducing signal loss caused by polarization mismatch and improving reception efficiency. When the $\vec{e}^{\,*}_R$ and $\vec{e}$ directions are aligned, that is, when the antenna's radiation direction completely matches the direction of the incident wave, the dot product reaches its maximum value. At this point, the *PLF* value is 1, indicating that the antenna has the highest received power and efficiency. To further broaden the bandwidth and improve the isolation between different polarized ports, Electric Dipoles and Magnetic Dipoles (ED&MDs) are combined in one antenna unit based on the dual-polarized antenna, as shown in Fig. 2.

In Fig. 2(a), an electric dipole is composed of two equal but oppositely numbered charges with a distance much smaller than the wavelength. An electric dipole is formed by extending a finite length of a current element in space. In Fig. 2(b), a magnetic dipole is composed of two magnetic charges that are very close together and of equal magnitude but different signs. A single magnetic charge does not exist, and magnetic dipoles are usually generated by current loops. The magnetic vector gener-

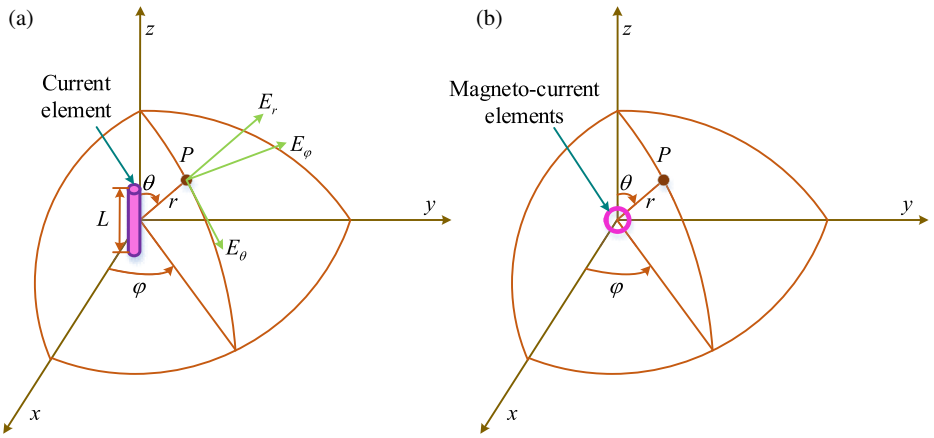

FIGURE 2. Schematic diagram of an electromagnetic dipole. (a) Electric dipoles. (b) Magnetic dipoles.

ated by the current element at point P is shown in Equation (3).

$$\begin{cases} k = \lambda\sqrt{\mu\varepsilon} \\ A = \frac{1}{4\pi}\int_{-\frac{L}{2}}^{\frac{L}{2}} \frac{I}{R} e^{-jkR} dz \end{cases} \tag{3}$$

In Equation (3), k is the wave number; A is the magnetic vector potential; j means the imaginary unit; μ and ε are the magnetic permeability and permittivity of the medium; I and L are the current intensity and length of the current element; R denotes the distance from the current element to the spatial point P; dz is an integral variable representing a small segment of the current element along its length. The far-field representation is obtained through magnetic vector analysis and calculation of electric dipole antennas, as shown in Equation (4).

$$\begin{cases} E_\theta = j\eta\frac{kIL}{4\pi r}\sin\theta e^{-jkr} \\ H_\varphi = j\frac{kIL}{4\pi r}\sin\theta e^{-jkr} \\ \eta = \sqrt{\frac{\mu}{\varepsilon}} \end{cases} \tag{4}$$

In Equation (4), E_θ is the electric field's component in the θ direction (perpendicular to the electric dipole) in the coordinate system; H_φ is the component of the magnetic field in the φ direction (parallel to the electric dipole) in the coordinate system; η is the characteristic impedance of the medium; r means the distance from the electric dipole to point P. The magnetic vector generated by the current loop at point P is shown in Equation (5).

$$A = \frac{1}{4\pi}\int_0^{2\pi} \widehat{\varphi}\frac{1}{R} e^{-jkR} d\varphi \tag{5}$$

In Equation (5), $\widehat{\varphi}$ is the unit vector in the direction of azimuth φ, and $d\varphi$ is an integral variable representing the azimuth angle on the current loop. Electric and magnetic fields can be converted into each other during electromagnetic wave propagation. Therefore, ED&MDs have similar radiation characteristics. The far-field representation of a magnetic dipole antenna is shown in Equation (6).

$$\begin{cases} E_\varphi = -j\frac{kI^mL}{4\pi r}\sin\theta e^{-jkr} \\ H_\theta = j\frac{kI^mL}{4\pi r\eta}\sin\theta e^{-jkr} \end{cases} \tag{6}$$

In Equation (6), m is a constant related to a specific parameter of the magnetic dipole. By combining ED&MDs, an diagram of equivalent circuit can be obtained, as displayed in Fig. 3.

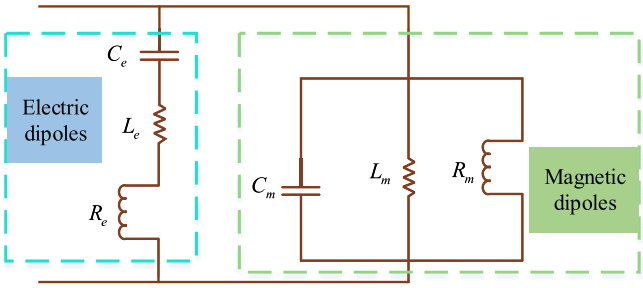

FIGURE 3. Equivalent circuit diagram.

In Fig. 3, a transmission line structure is formed by alternately connecting two transmission lines with different characteristic impedances. By connecting ED&MDs in parallel, the bandwidth is widened. The equivalent circuit model reveals the underlying mechanism of magnetic dipole broadband characteristics theoretically, providing a quantifiable parameter optimization basis for antenna design. Although the process of directly driving design decisions is not described in detail, this model provides theoretical support for optimizing magnetic dipole broadband antennas. This also explains why this structure can break through the bandwidth limitations of traditional antennas, making the design physically reasonable and operable. The equivalent circuit model of the MED antenna can be used for designing and analyzing antennas, as shown in Equation (7).

$$Y_{in} \approx Y_a = \left(\frac{1}{R_e} + \frac{1}{R_m}\right) - j\left[\left(\lambda L_e - \frac{1}{\lambda C_e}\right)\frac{1}{R_e^2} - \left(\lambda C_m - \frac{1}{\lambda L_m}\right)\right] \tag{7}$$

In Equation (7), Y_{in} is the input admittance of the antenna; Y_a is the approximate input admittance of the antenna; R_e/R_m,

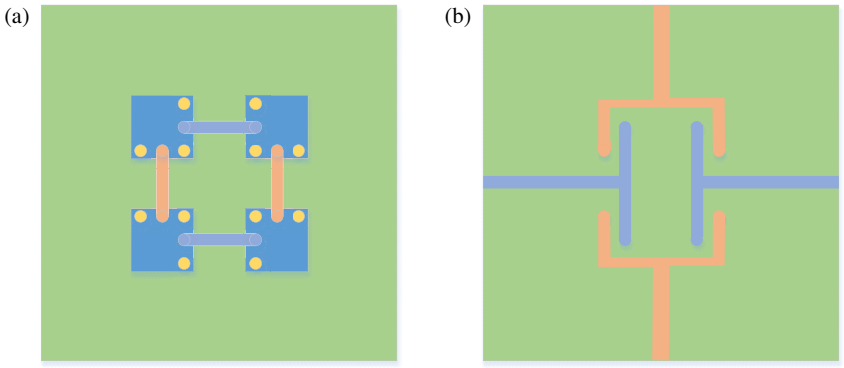

FIGURE 4. Patch structure diagram. (a) Top view. (b) Bottom view.

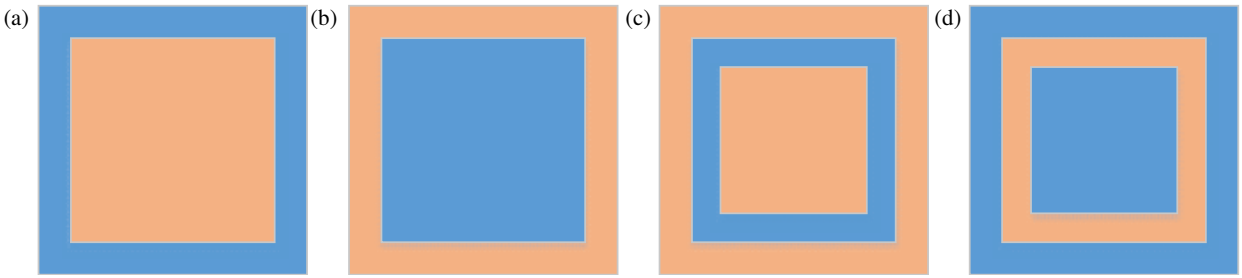

FIGURE 5. Structural diagram of a meta-surface. (a) Low-pass filtering characteristics. (b) High-pass filtering characteristics. (c) Band resistance filtering characteristics. (d) Bandpass filtering characteristics.

L_e/L_m, and C_e/C_m are the radiation resistances, inductances, and capacitances of ED&MDs. The input admittance of MED antenna is composed of parallel input admittance of electric dipole and magnetic dipole. Due to the different frequencies of ED&MDs, their parallel combination can achieve good impedance matching over a wide frequency range, thereby providing a wide matching bandwidth. By adjusting the electrical parameters of the antenna, a wider operating bandwidth can be obtained, as shown in Equation (8).

$$\begin{cases} C_e L_e = C_m L_m \\ R_e^2 = \frac{L_e}{C_m} \end{cases} \tag{8}$$

In Equation (8), $C_e L_e = C_m L_m$ is the resonant frequency of the electric dipole and the magnetic dipole, which are equal and operate at the same frequency to achieve complementarity. $R_e^2 = \frac{L_e}{C_m}$ is the impedance matching between ED&MDs, resulting in a wider operating bandwidth. By satisfying these two conditions, the bandwidths of ED&MDs can be combined to obtain a wider matching bandwidth, thereby achieving broadband and good impedance matching.

2.2. Broadband Dual-Polarization MWA Based on Metasurface Optimization

Broadband dual-polarization MWA is an antenna that can radiate or receive electromagnetic waves in two orthogonal polarization directions. It has significant advantages such as easy integration and stability in WC, but still faces the limitation of low gain [15, 16]. Metasurfaces regulate the amplitude, phase, polarization, and other characteristics of electromagnetic waves at sub-wavelength scales. Therefore, this study introduces metasurfaces into broadband dual-polarization MWA and proposes BDMW-MA, which further improves the dual-polarization performance of the antenna by improving the geometry, size, and arrangement of the patch [17]. In practical applications, the common dual-polarized MWA patch structure is exhibited in Fig. 4.

Figure 4(a) shows the antenna's planar layout viewed from top to bottom, with two electric dipoles connected by a feeding structure. Fig. 4(b) shows the planar layout of the antenna viewed from bottom to top, with metalized holes serving as radiating elements to enhance the antenna's radiation capability. The radiation characteristics of broadband dual-polarized millimeter waves are achieved through the combination of ED&MDs. Metallized holes act as equivalent magnetic dipoles and work in conjunction with electric dipoles to achieve the desired electromagnetic properties. In Fig. 4, the electric dipoles are orthogonal rectangular strips with a length of 3.2 mm and a width of 0.6 mm. The metallized holes have a diameter of 0.3 mm, and there are four of them. The copper thickness is 35 µm; the dielectric substrate thickness is 0.254 mm; the dielectric constant is 2.2. The characteristic impedance of the feedline is 50 Ω, and the input impedance of the radiating patch is matched to 50 Ω. The design freedom of metasurface antennas is high, and different electromagnetic characteristics can be achieved by changing the unit structure and arrangement. The metasurface structure is shown in Fig. 5.

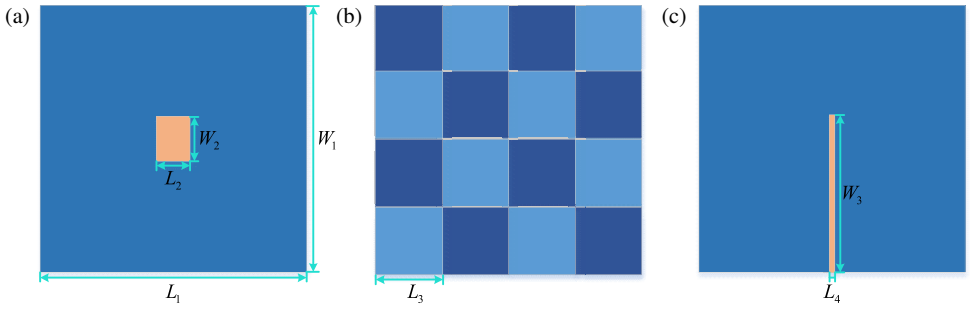

FIGURE 6. Schematic diagram of each layer of the antenna. (a) Top floor. (b) Interlayer. (c) Underlying.

Figure 5(a) shows the low-pass unit of a Frequency Selective Surface (FSS), which allows signals below a certain cutoff frequency to pass through, while signals above that frequency are reflected or absorbed. Fig. 5(b) shows a high-pass cell that allows signals above a certain cutoff frequency to pass through, while signals below that frequency are reflected or absorbed. Fig. 5(c) shows a bandpass unit that allows signals between two cutoff frequencies to pass through, while signals at other frequencies are reflected or absorbed. Fig. 5(d) shows a band-stop unit that allows signals of frequencies other than those between two cutoff frequencies to pass through, while signals within that frequency band are reflected or absorbed [18]. The metasurface band-rejection unit in Fig. 5 consists of complementary metal square ring structures with a line width of 0.2 mm, arranged in a 2×4 pattern to form an array of eight units. The dielectric layer thickness is 0.127 mm; the copper thickness is 17 µm; the equivalent refractive index is 1.5–2.0. To reduce external interference while maintaining the antenna's performance within the operating frequency band, a band-stop unit improvement patch is selected, as shown in Equation (9).

$$T = \begin{bmatrix} \cos(nkd) & -\frac{w}{k}\sin(nkd) \\ \frac{w}{k}\sin(nkd) & \cos(nkd) \end{bmatrix} \tag{9}$$

In Equation (9), $\cos(nkd)$ and $\sin(nkd)$ are the phase changes of electromagnetic waves on the metasurface; n is the equivalent refractive index; k denotes the wave number; d is the thickness of the equivalent optically active material; w means the equivalent impedance. Therefore, the patch with improved metasurface is shown in Fig. 6.

Figure 6(a) shows a rectangular metal radiation patch responsible for emitting and receiving electromagnetic waves. In Fig. 6(b), the middle layer of the antenna is composed of 8 square element arrays, which are utilized to control the propagation of electromagnetic waves. Fig. 6(c) shows a metal feeder line responsible for transmitting signals from the feeding point of the antenna to the radiating patch. In Fig. 6, the top-layer radiating patch is a 6 mm $\times$ 5 mm rectangular metal patch with a copper thickness of 35 µm and is centrally placed. The intermediate metasurface layer consists of a 2×4 band-rejection unit array with a dielectric thickness of 0.127 mm, a copper thickness of 35 µm, a distance from the feedline layer dielectric thickness of 0.254 mm, and a total thickness of 0.635 mm. The S parameter directly reflects the reflection and transmission characteristics of the network. By calculating the transmission matrix of each layer and multiplying these matrices, the total transmission matrix of the entire structure is obtained. Finally, the S parameter is calculated as shown in Equation (10).

$$S_{12} = S_{21} = \frac{1}{\left[\sin(nkd) - \frac{i}{2}\left(w + \frac{1}{w}\cos(nkd)\right)\right] e^{ikd}} \tag{10}$$

In Equation (10), S_{12} and S_{12} are non-diagonal elements of the S-parameter matrix, and i is the imaginary unit. Port 1 and Port 2 are the two ports used to characterize signal input and output in a metasurface antenna structure. Port 1 serves as the signal input port, responsible for transmitting the excitation signal into the metasurface structure, acting as the starting point for electromagnetic waves entering the antenna system. Port 2 serves as the signal output port, used to receive electromagnetic wave signals modulated by the metasurface, and as the output port for structurally processed signals. In addition, the calculation for the diagonal of the S-parameter matrix is shown in Equation (11).

$$S_{11} = S_{22} = \frac{i}{2}\left(\frac{1}{Z} - Z\right)\sin(nkd) \tag{11}$$

In Equation (11), S_{11} and S_{22} are diagonal elements of the S-parameter matrix, and Z is the characteristic impedance of the port. The equivalent refractive index of the meta-surface is further calculated using the S-parameter, as shown in Equation (12).

$$n = \frac{1}{kd}\cos^{-1}\left[\frac{1}{2S_{21}}\left(1 - S_{11}^2 + S_{21}^2\right) + 2\pi q\right] \tag{12}$$

In Equation (12), q is an integer used to ensure that the refractive index n is a real number. In addition, the impedance of the metasurface is shown in Equation (13).

$$Z = \sqrt{\frac{(1 + S_{11})^2 - S_{21}^2}{(1 - S_{11})^2 - S_{21}^2}} \tag{13}$$

In Equation (13), converting the S-parameter into the physical properties of the metasurface can more intuitively and effectively design and optimize the metasurface structure. The dielectric constant is used to describe parameters, and the propagation characteristics of electromagnetic waves are further controlled by adjusting the parameters, as shown in Equation (14).

$$\varepsilon = \frac{n}{Z} \tag{14}$$

TABLE 1. Experimental testing equipment and its key parameters.

Laboratory equipment	Parameters	Effect
Vector network analyzer	Frequency Range: 20–50 GHz; Dynamic Range: $\geq$ 120 dB; Measurement Accuracy: $\leq$ 0.1 dB; Port Impedance: 50 Ω	Measure the antenna frequency characteristics
Microwave anechoic chamber	Dimensions: 5 m × 5 m × 5 m; Absorber Material Performance: Reflectivity ≤ -20 dB within the 20–50 GHz frequency band; Isolation: $\geq$ 60 dB	Provide a non-reflective electromagnetic environment
Antenna test turntable	Rotation range: 0–360°; Rotation accuracy: ±0.1°; Load capacity: 50 kg	Secure the antenna and control its rotation angle
Signal source	Frequency range: 20–50 GHz; Output power: $\geq$ 10 dBm; Frequency stability: $\leq$ 10 ppm	Provide millimeter-wave test signals
Spectrum analyzer	Frequency Range: 20–50 GHz; Resolution Bandwidth: 1 Hz–1 MHz; Dynamic Range: $\geq$ 100 dB	Analyze antenna signal spectrum

TABLE 2. Comparison of antenna performance.

Antenna	Matching Efficiency	Reflection Coefficient	Radiation Efficiency	Total Transmission Efficiency (TTE)
A1	0.88	0.11	0.45	0.43
A2	0.90	0.09	0.51	0.49
A3	0.75	0.18	0.39	0.35
A4	0.97	0.04	0.70	0.68

In Equation (14), ε is the equivalent dielectric constant. In addition, the expression of parameters using magnetic permeability is shown in Equation (15).

$$\mu = nZ \tag{15}$$

In Equation (15), μ is the equivalent magnetic permeability. It achieves the directional manipulation of electromagnetic waves by adjusting the equivalent refractive index n and relative impedance Z, thereby changing ε and μ.

3. RESULTS

3.1. Performance Testing of BDMW-MA

To evaluate the comprehensive performance of BDMW-MA, a comparative experimental setup is designed. The experimental equipment used is listed in Table 1.

As shown in Table 1, experiments conducted using these devices enable the precise control of experimental variables, minimizing the impact of environmental factors on antenna performance. Additionally, four representative broadband millimeter-wave antennas are selected as the control group. A1 (Single-Polarized Broadband Millimeter-Wave Meta-surface Antenna): Radiating patch 3.2 mm × 0.8mm; Two-layer dielectric substrate (each 0.254 mm and 0.127 mm thick); Ground plane 10 mm×10 mm; 50 Ω feedline, with width of 0.3 mm and length of 5.5 mm; Bandwidth 20–45 GHz. A2 (Traditional Array Broadband Dipole Millimeter-Wave Antenna): 2 × 2 array; Units are orthogonal rectangles (3 mm × 3.2 mm); Spacing 4.3 mm; Dielectric substrate thickness 0.254 mm; Dual-port 50 Ω feedline, with width of 0.3 mm; Bandwidth 22–48 GHz. A3 (Basic Broadband Millimeter-Wave Patch Antenna): Radiating patch is a 2.8 mm × 3.5 mm rectangle; Copper thickness 35 µm; Dielectric substrate thickness 0.127 mm; Dielectric constant 2.2; 50 Ω feedline, with width of 0.28 mm and length of 5 mm; Bandwidth 25–40 GHz. A4 (Broadband Dual-Polarization Millimeter-Wave Meta-surface Antenna): Orthogonal electric dipoles (3.2 mm × 0.6 mm); Spacing 1.5 mm, with 0.3 mm metallized holes at both ends; 2 × 4 band-reject meta-surface array (outer ring 2.5 mm, inner ring 1.5 mm); Three-layer dielectric substrate (0.254 mm, 0.127 mm, and 0.254 mm thick); Dual-port 50 Ω feedline, with a width of 0.32 mm; Bandwidth of 20–50 GHz; Superstructure stopband of 30–35 GHz. Experimental tests are conducted on the performance of four types of antennas, as shown in Table 2.

In Table 2, A3 performs the worst in terms of matching efficiency, reflection coefficient, radiation efficiency, and TTE, with values of 0.75, 0.18, 0.39, and 0.35, respectively. A4 performs the best in terms of performance metrics, with values of 0.97, 0.04, 0.70, and 0.68, respectively. Comparison shows that among the four antennas, BDMW-MA has the highest matching efficiency, radiation efficiency, and TTE, with the lowest reflection coefficient, indicating that BDMW-MA has good performance and low loss during transmission. In addition, to verify the gain performance of BDMW-MA, experiments are conducted on A1, A2, A3, and A4 using electromagnetic simulation software at frequencies of 25–50 GHz, as shown in Fig. 7.

In Fig. 7(a), simulation results show that A1 exhibits a gain of 5.2 dBi at 25 GHz, with an overall trend of increasing then decreasing, reaching a peak value of 6.1 dBi at 35 GHz. Within the 25–50 GHz frequency range, A2 exhibits a maximum gain

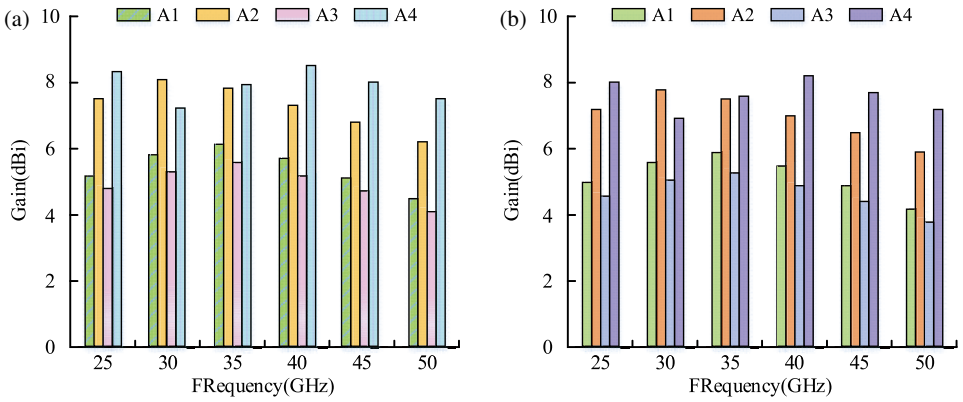

FIGURE 7. Comparison of test results and expected differences in antenna gain at 25–50 GHz. (a) Simulation. (b) Actual measurement.

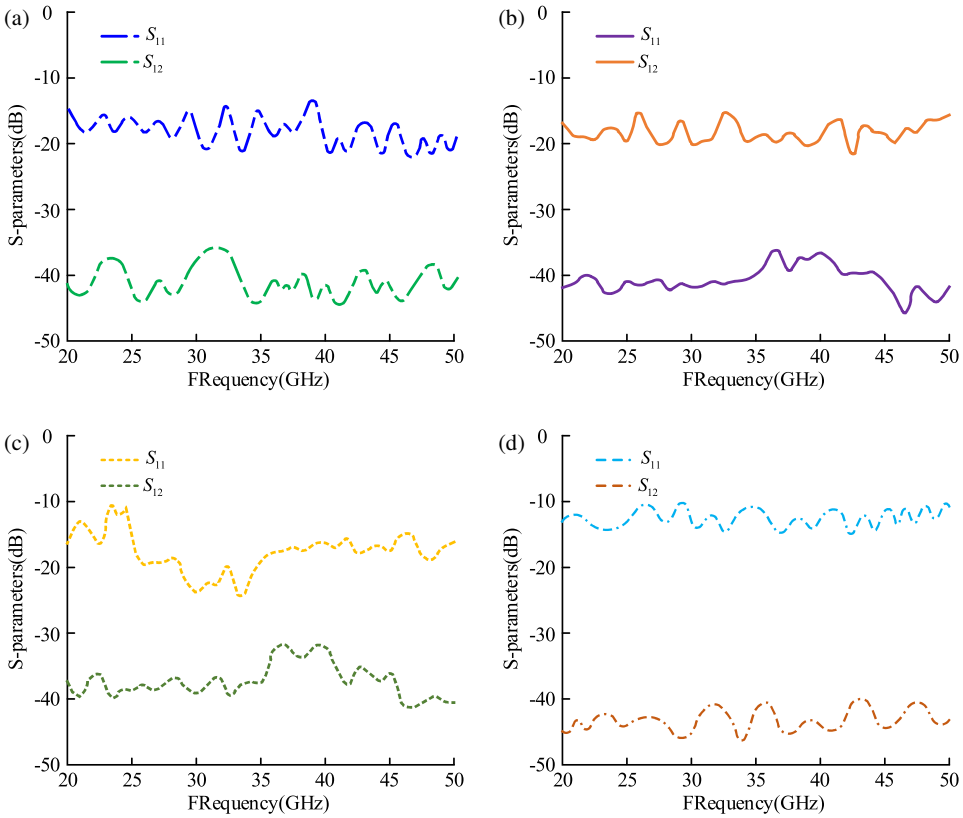

FIGURE 8. Comparison of antenna S-parameter test results and expected differences between 20–50 GHz. (a) The reflection coefficient of A1. (b) The reflection coefficient of A2. (c) The reflection coefficient of A3. (d) The reflection coefficient of A4.

of 8.1 dBi, differing by 1.9 dBi from its minimum value. A3's gain fluctuates within the range [5.6 dBi, 4.1 dBi]. A4's minimum gain is 7.2 dBi, with gains exceeding the reference antenna at most frequency points. In Fig. 7(b), the measured gain of A1 gradually increases from 5.0 dBi at 25 GHz before decreasing to 4.2 dBi at 50 GHz. A2 exhibits a gain of 7.2 dBi at 25 GHz and 5.9 dBi at 50 GHz. A3 demonstrates the lowest gain among the four antennas, with a maximum gain of only 5.3 dBi. A4 maintains a consistently high gain level, fluctuating within the range [6.9 dBi, 8.2 dBi]. These data indicate that the simulation results align with the measured trends, with A4 demonstrating superior gain performance across the broadband spectrum compared to the reference antennas. This confirms the superiority of broadband dual-polarization millimeter-wave metasurface structures in enhancing antenna gain. To verify the isolation level of BDMW-MA, experiments are conducted on A1, A2, A3, and A4 at frequencies of 20–50 GHz, as shown in Fig. 8.

In Fig. 8(a), the S_{11}-curve of A1 exhibits significant fluctuations, with an overall trend near -18 dB, and the maximum difference between extremes is -10 dB. The S_{12}-curve exhibits significant fluctuations, with an overall trend near -40 dB, and the maximum difference between extremes is -10 dB. In Fig. 8(b), the S_{11}-curve of A2 exhibits significant

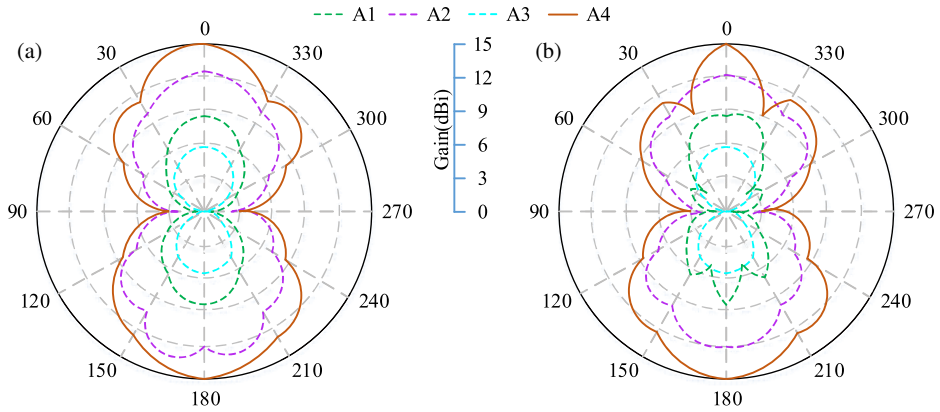

FIGURE 9. Comparison of the radiation direction of the antenna. (a) E-side. (b) H-side.

fluctuations, with an overall fluctuation around -19 dB, and the maximum difference between extremes is -8 dB. The S_{12}-curve exhibits significant fluctuations, with an overall fluctuation around -40 dB, and the maximum difference between extremes is -10 dB. In Fig. 8(c), the S_{11}-curve of A3 has significant fluctuations, with an overall fluctuation close to -20 dB and a maximum extreme difference of -15 dB. The S_{12}-curve has significant fluctuations, with an overall fluctuation close to -35 dB and a maximum extreme difference of -10 dB. In Fig. 8(d), the S_{11}-curve of A4 has relatively small fluctuations, with an overall fluctuation close to -12 dB and a maximum extreme difference of -5 dB. The S_{12}-curve has small fluctuations, with an overall fluctuation close to -44 dB and a maximum extreme difference of -7 dB. Experimental verification shows that BDMW-MA has a high degree of isolation, further demonstrating that the proposed antenna has strong signals and high accuracy.

3.2. Application Effect Testing of BDMW-MA

To verify the anti-interference ability of BDMW-MA, the TTE of four antennas A1 to A4 is tested when the Signal-to-Noise Ratio (SNR) is 0, 10, 20, 30, 40, and 50 dB, as shown in Table 3.

TABLE 3. Performance testing of different models.

Antenna	0 dB	10 dB	20 dB	30 dB	40 dB	50 dB
A1	0.26	0.40	0.46	0.48	0.50	0.55
A2	0.34	0.43	0.49	0.50	0.54	0.59
A3	0.20	0.31	0.38	0.39	0.45	0.51
A4	0.44	0.62	0.70	0.72	0.79	0.85

In Table 3, when SNR $=$ 0 dB, the minimum TTE of A3 is 0.20, and the maximum TTE of A4 is 0.44. When SNR $=$ 20 dB, the TTE of A1–A4 is (0.46, 0.49, 0.38, and 0.70). When SNR $=$ 30 dB, the maximum TTE of A4 is 0.70. When SNR $=$ 40 dB, the TTE of A1$\sim$A4 is (0.50, 0.54, 0.45, and 0.79). When SNR $=$ 50 dB, the maximum TTE of A4 is 0.85. The data show that when the SNR is below 10 dB, the overall transmission efficiency of the antenna significantly decreases. In different SNR environments, the overall transmission efficiency of BDMW-MA is always the highest, indicating its strong anti-interference ability. To verify the high gain performance of BDMW-MA, 10 experiments are conducted to record the radiation directions of A1, A2, A3, and A4 in the E-plane and H-plane at 35 GHz, as shown in Fig. 9.

In Fig. 9(a), A1 exhibits relatively high gain values near 0° and 180°, at 8.1 dBi and 8.4 dBi, respectively. As the angle shifts toward 90° and 270°, the gain decreases, with the overall gain level remaining at an intermediate level and a relatively wide beam coverage range. A2 has higher gain than A1, with distinct gain peaks near 0° and 180°. The gain decreases more rapidly than A1 as the angle deviates, and the beam is narrower than A1's. The gain of the A3 curve is the lowest, with relatively small gain values at all angles, and the gain changes more smoothly with the angle, resulting in the widest beam coverage range. A4 has higher gain than A1, A2, and A3, with prominent gain peaks near 0° and 180°, at 14.9 dBi and 15.0 dBi, respectively. Gain decreases as the angle deviates from the main direction, and the beam is the narrowest among the four curves. In Fig. 9(b), A1 gain fluctuates with angle changes, with overall gain levels similar to A1 on the E-plane and a relatively wide beam coverage range. A2 has relatively high gain values at multiple angles, with a narrow beamwidth. The gain of the A3 curve is the lowest, and the gain values at all angles are very small. The gain changes relatively steadily with the angle, and the beam coverage range is the widest. A4 has the highest gain among the four curves, with a significant gain peak of 15.0 dBi near the main angle. The main gain decreases as the angle deviates, and the beamwidth is the narrowest among the four curves. The comparison demonstrates that the BDMW-MA possesses high gain and high directivity performance, enabling concentrated radiation of energy in specific directions, which is advantageous for long-distance signal transmission and reception. In addition, to verify the gain of BDMW-MA, a vector network analyzer is used to test the antenna, and experiments are conducted on BMWPA and BDMW-MA at temperatures of -50, 0, and 50°C, as shown in Fig. 10.

In Fig. 10(a), when the temperature is -50°C, the gain curve of BMWPA fluctuates greatly, with a maximum difference value of 6 dBi between extreme values. When the temperature is 0°C and 50°C, the gain curve of BMWPA has small fluctuations, with maximum difference values of 4 dBi and 3 dBi

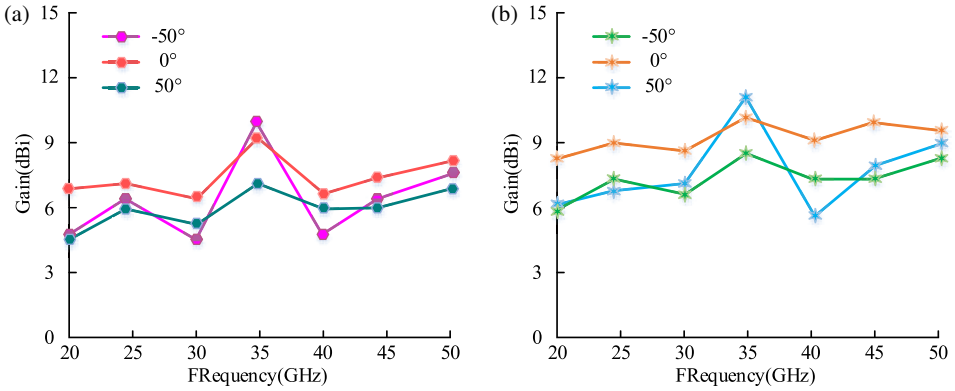

FIGURE 10. S-parameter curve of the antenna. (a) Gain curve of A3. (b) Gain curve of A4.

between extreme values. In Fig. 10(b), when the temperature is $-50°$C, the gain curve of BDMW-MA fluctuates greatly, with a maximum difference value of 5 dBi between extreme values. When the temperature is 0°C and 50°C, the gain curve of BDMW-MA has small fluctuations and is generally stable, with the maximum difference values between extreme values being 3 dBi. Comparison shows that low temperature has an obvious effect on the performance of the antenna. BDMW-MA has less gain variation at different temperatures and has high reliability and stability, with a wide range of application scenarios.

4. DISCUSSION AND CONCLUSION

4.1. Discussion

This study optimized BMWPA through MED and introduced a metasurface with band-stop units, ultimately designing a BDMW-MA. By testing the performance of the proposed antenna in WC and conducting comparative experiments, a considerable amount of data results were obtained, and further research and exploration were conducted based on the experimental results. The matching efficiency, reflection coefficient, radiation efficiency, and TTE of BDMW-MA were 0.97, 0.04, 0.70, and 0.68. The data showed that the WC performance of the designed antenna was superior to other compared antennas, meeting the performance requirements of WC for antennas. In the comparison of BDMW-MA using electromagnetic simulation software, the gain curve under the test experiment fluctuated similarly to the gain curve under the simulation experiment, with a maximum distance of 2 dBi between the two. The high isolation of the designed antenna was further verified by testing the S-parameters of BDMW-MA. The curve had small fluctuations and was generally gentle, fluctuating around -12 dB with a maximum extreme difference of -5 dB. The curve had small fluctuations and fluctuated around -45 dB with a maximum extreme difference of -10 dB. Various experiments have shown that the designed antenna has superiority, but there is still a problem of complex structural calculations, and it is considered to replace the dielectric material for improvement. Karthikeyan et al. designed and compared substrates with variable relative permittivity values, and obtained suitable dielectric materials through experiments on different dielectric materials and patch shapes of the substrate [19]. Compared with the CMC-based electronic devices designed by Gallegos-Rosas et al., the manufacturing of BDMW-MA is more complex but more stable, meeting the strict high-frequency performance requirements of millimeter wave communication. This is a performance level that simplified CMC devices cannot match. In terms of size, the antenna's compact design, which strictly matches the wavelength, is a key to achieving efficient signal transmission in scenarios such as 5G and autonomous driving. However, CMC devices, with their flexible large-size design, are more suitable for low-speed flexible electronics and cannot meet the miniaturization and directionality requirements of high-frequency communication. In terms of cost, while antennas have higher costs due to specialized materials and precision manufacturing, their high transmission efficiency (0.68) and low reflection coefficient (0.04) provide significant communication performance gains, making them indispensable in fields with extremely high requirements for transmission quality [20]. In summary, BDMW-MA based on MED has good performance in WC, high application value, and development prospects, and can further improve the quality of WC.

5. CONCLUSION

In response to issues such as bandwidth, size limitations, and low adaptability, this study adopted MED-optimized BMWPA, and on this basis, introduced metasurfaces to further improve the gain and dual-polarization performance of the antenna, and designed BDMW-MA. In comparative verification, when the SNR was 0 dB, 10 dB, 20 dB, 30 dB, 40 dB, and 50 dB, the TTE of the studied antenna was 0.44, 0.62, 0.70, 0.72, 0.79, and 0.85. In addition, 10 sets of experiments were conducted to test the gain of the designed antenna. The BDMW-MA showed significantly higher gain than the reference antenna in the radiation patterns of the E-plane and H-plane. The gain peak in the E-plane was 15.0 dBi, with the narrowest beam. Similarly, the H-plane also had the highest gain of 15.0 dBi, and the beamwidth was the narrowest among the four curves. Experimental results show that in practical applications, the designed antenna has high accuracy, good stability, high gain, minimal loss during signal transmission, and strong anti-interference ability. However, losses during signal transmission are inevitable and require material improvement. Future research needs to design more efficient antennas for verification.

REFERENCES

[1] Tu, Z.-H., W.-S. Ou, and F.-C. Chen, "Compact isolation-enhanced dual-band $\pm 45^{\circ}$ polarization beam-scanning millimeter-wave antennas with dual-band bandstop structures," *IEEE Transactions on Antennas and Propagation*, Vol. 72, No. 6, 5373–5378, 2024.

[2] Wu, F., "Research on the application of novel antenna design in millimeter-wave communication," *Computing, Performance and Communication Systems*, Vol. 8, No. 1, 25–30, 2024.

[3] Ueno, Y., Y. Tomida, T. Tanimoto, M. Tanaka, Y. Tabuchi, K. Inoue, and H. Nakamura, "Inter-temperature bandwidth reduction in cryogenic QAOA machines," *IEEE Computer Architecture Letters*, Vol. 23, No. 1, 9–12, 2024.

[4] Wu, W., K.-D. Xu, Q. Chen, T. Tanaka, M. Kozai, and H. Minami, "A low-cost wideband reflectarray antenna based on non-radiative dielectric waveguide," *IEEE Antennas and Wireless Propagation Letters*, Vol. 22, No. 12, 3152–3156, 2023.

[5] Junior, J. G. D., A. G. D'Assuncao, and V. P. S. Neto, "A new efficient dual-band circularly polarized implantable patch antenna for wireless power transfer," *IEEE Antennas and Wireless Propagation Letters*, Vol. 24, No. 2, 294–298, 2025.

[6] Wan, P., D. Chen, D. Wang, X. Hui, and K. Peng, "Gamma approximation based multi-antenna covert communication detection," *China Communications*, Vol. 21, No. 9, 90–97, 2024.

[7] Nagar, D., P. Ranjan, and A. Chowdhury, "Flexible metasurface loaded felt substrate built wearable antenna with tri-band and high gain features for WBAN applications," *Journal of Electronic Materials*, Vol. 54, 5918–5927, 2025.

[8] Wang, Y., J. Shi, and J. Wang, "Wearable antenna sensor based on EBG structure for human body area humidity monitoring," *IEEE Sensors Journal*, Vol. 24, No. 3, 3833–3843, 2024.

[9] Battaglia, G. M., G. G. Bellizzi, A. F. Morabito, G. Sorbello, and T. Isernia, "A general effective approach to the synthesis of shaped beams for arbitrary fixed-geometry arrays," *Journal of Electromagnetic Waves and Applications*, Vol. 33, No. 18, 2404–2422, 2019.

[10] Fang, B., Z. Wang, Y. Li, J. Ji, K. Xi, Q. Cheng, F. Shu, Z. Jin, Z. Hong, C. Zhan, C. Shen, and T. Li, "Spin-decoupled metacoupler empowered multiplexing and multifunction of guided wave radiation," *Photonics Research*, Vol. 11, No. 12, 2194–2201, 2023.

[11] Tang, S.-C., Z. Liang, X.-Y. Wang, J.-X. Chen, Y. Pan, and S. Zheng, "Integrated-antenna-filter based on metal-dielectric heterogeneous resonator," *IEEE Transactions on Antennas and Propagation*, Vol. 73, No. 3, 1864–1869, 2025.

[12] Cui, S., Y. Li, S. Zhang, L. Chen, C. Cao, and D. Su, "A polarization control operator for polarized electromagnetic wave designing," *Chinese Journal of Electronics*, Vol. 33, No. 5, 1253–1260, 2024.

[13] Zhu, Z., Y. Li, Z. Qin, L. Jiang, W. Wang, H. Chen, J. Wang, Y. Pang, and S. Qu, "Miura origami based reconfigurable polarization converter for multifunctional control of electromagnetic waves," *Photonics Research*, Vol. 12, No. 3, 581–586, 2024.

[14] Tang, B., K. Ma, E. N. Moro, and Y. Luo, "Design of differential multi-point feeding dual-polarized SISL antenna based on CM analysis," *Chinese Journal of Electronics*, Vol. 33, No. 5, 1245–1252, 2024.

[15] Bandewad, G., K. P. Datta, B. W. Gawali, and S. N. Pawar, "Review on discrimination of hazardous gases by smart sensing technology," *Artificial Intelligence and Applications*, Vol. 1, No. 2, 70–81, 2023.

[16] Sun, Y., H.-T. Hu, and C. H. Chan, "Millimeter-wave wideband, high-gain, dual-polarized filtering patch antenna with Y-shaped probe and shorted C-shaped strip," *IEEE Transactions on Antennas and Propagation*, Vol. 72, No. 11, 8816–8821, 2024.

[17] Hu, Y., J. Zhang, E. Shi, Y. Lu, J. An, C. Yuen, and B. Ai, "Joint beamforming and power allocation design for stacked intelligent metasurfaces-aided cell-free massive MIMO systems," *IEEE Transactions on Vehicular Technology*, Vol. 74, No. 3, 5235–5240, 2025.

[18] Liang, C., W. Yang, Q. Xue, W. Che, and H. Wong, "Wideband high-transparent dipole antenna based on frequency selective surface and its applications in dual-band shared-aperture array," *IEEE Antennas and Wireless Propagation Letters*, Vol. 24, No. 3, 572–576, 2025.

[19] Karthikeyan, T. A., M. Nesasudha, and M. L. Valarmathi, "Investigations on flexible dielectric material-based wearable antenna for tumor detection," *Journal of Materials Science: Materials in Electronics*, Vol. 35, No. 35, 2226, 2024.

[20] Gallegos-Rosas, K., A. Azari, and C. Soldano, "Carboxymethyl cellulose as a sustainable dielectric material for organic field-effect transistors," *ACS Applied Electronic Materials*, Vol. 7, No. 3, 1274–1282, 2025.